Materials Reports: Energy xxx (xxxx) xxx

Contents lists available at ScienceDirect

Materials Reports: Energy

journal homepage: www.keaipublishing.com/en/journals/materials-reports-energy

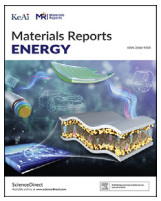

Original Research Report

Electro-assisted photocatalytic reduction of CO_2 in ambient air using Ag/TNTAs at the gas-solid interface

Feng Yue [a], Zhaoya Fan [a], Cong Li [a,c], Yang Meng [a], Shuo Zhang [a], Mengke Shi [a], Minghua Wang [a], Mario Berrettoni [c], Jun Li [b,**], Hongzhong Zhang [a,*]

[a] Henan Collaborative Innovation Center of Environmental Pollution Control and Ecological Restoration, Zhengzhou University of Light Industry, Zhengzhou, 450001, PR China

[b] Henan Institute of Advanced Technology, Zhengzhou University, Zhengzhou, 450052, PR China

[c] Department of Chemistry, University of Camerino, Camerino, 62032, Macerata, Italy

ARTICLE INFO

Keywords:
Electro-assisted photocatalytic
Gas-solid interface
Ambient air
P–N heterojunction
Practical applications

ABSTRACT

The direct conversion of atmospheric CO_2 into fuel via photocatalysis exhibits significant practical application value in advancing the carbon cycle. In this study, we established an electro-assisted photocatalytic system with dual compartments and interfaces, and coated Ag nanoparticles on the titanium nanotube arrays (TNTAs) by polydopamine modification. In the absence of sacrificial agent and alkali absorption liquid conditions, the stable, efficient and highly selective conversion of CO_2 to CO at the gas-solid interface in ambient air was realized by photoelectric synergy. Specifically, with the assistance of potential, the CO formation rates reached 194.9 μmol h^{-1} m^{-2} and 103.9 μmol h^{-1} m^{-2} under ultraviolet and visible light irradiation, respectively; the corresponding CO_2 conversion rates in ambient air were 30% and 16%, respectively. The excellent catalytic effect is mainly attributed to the formation of P–N heterojunction during the catalytic process and the surface plasmon resonance effect. Additionally, the introduction of solid agar electrolytes effectively inhibits the hydrogen evolution reaction and improves the electron utilization rate. This system promotes the development of photocatalytic technology for practical applications and provides new insights and support for the carbon cycle.

1. Introduction

Over the past century, the extensive use of traditional fossil fuels has led to a significant increase in carbon dioxide (CO_2) emissions, resulting in a multitude of environmental issues and energy crises.[1–4] In light of resource and environmental considerations, CO_2 represents a readily available and abundant carbon resource.[5] In particular, it is proposed that the largest domestic CO_2 emission is currently coal-fired boiler flue gas, with a concentration of about 11%–15%. Therefore, CO_2 is directly used as a reactant in a low-concentration CO_2 or even ambient air atmosphere, and photocatalytic technology is used to efficiently convert it into C_1/C_2 fuel, providing a promising, practical application prospect, cost-effective, economic and environmentally friendly strategy.[6–13] For instance, carbon monoxide (CO) is a valuable resource with applications as a fuel and cornerstone in one-carbon chemistry within the chemical industry. CO plays a vital role as a primary raw material in the synthesis of a wide range of fundamental organic chemical products and intermediates. Starting from CO, a vast array of essential chemicals can be synthesized, including ammonia, phosgene, alcohols, acids, anhydrides, esters, aldehydes, ethers, amines, alkanes, and olefins. Moreover, the properties of carbonyl metal complexes or their derivatives, formed through the reaction of CO with transition metals, can be utilized to prepare various homogeneous catalysts required for organic chemical production. The utilization of efficient photocatalysts to transform these compounds into value-added products offers a viable solution to potential environmental challenges and energy crises.[14–16] This approach

* Corresponding author.
** Corresponding author.
E-mail addresses: junli2019@zzu.edu.cn (J. Li), zhz@zzuli.edu.cn (H. Zhang).

Production and Hosting by Elsevier on behalf of KeAi

https://doi.org/10.1016/j.matre.2024.100269
Received 11 November 2023; Received in revised form 18 January 2024; Accepted 29 January 2024
Available online xxxx

Please cite this article as: Yue F et al., Electro-assisted photocatalytic reduction of CO_2 in ambient air using Ag/TNTAs at the gas-solid interface, Materials Reports: Energy, https://doi.org/10.1016/j.matre.2024.100269

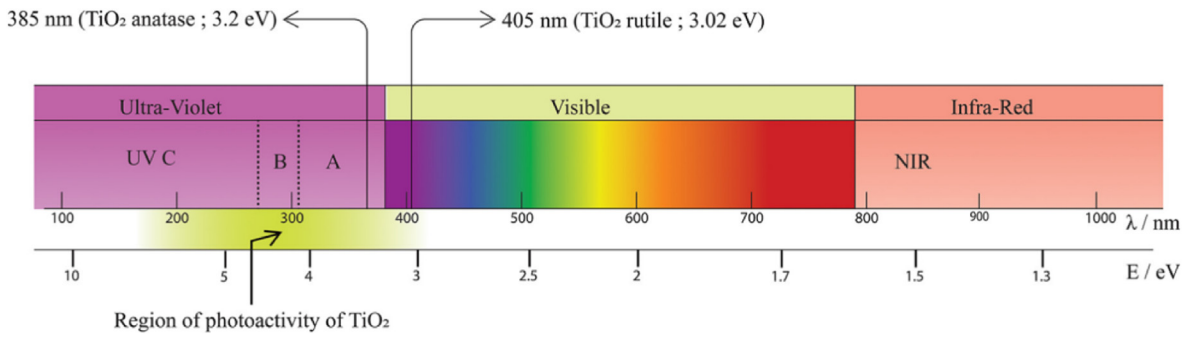

Fig. 1. Absorption spectrum for the photocatalytic activity of TiO_2. Reproduced with permission from Ref. 25.

holds paramount strategic significance for energy conservation, emission reduction, and the promotion of a low-carbon economy. Consequently, numerous common semiconductor materials, such as titanium dioxide (TiO_2), copper oxide (CuO), graphitic carbon nitride (g-C_3N_4), cuprous oxide (Cu_2O),[17] cadmium sulfide (CdS)[18] and bismuth (Bi)-based materials, have been employed as promising photocatalysts for CO_2 conversion via photocatalytic reduction.[19]

Among various photocatalysts, TiO_2 has been widely utilized in photocatalysis due to its chemical stability and low cost. However, there are still significant challenges in pure TiO_2-based photocatalysis.[20–23] One of the primary limitations is its relatively wide bandgap, which restricts the material's photoexcitation activation to ultraviolet (UV) radiation. As illustrated in Fig. 1, solar radiation comprises 49% infrared, 46% visible, and only 5% UV radiation. Consequently, pure TiO_2 cannot fully harness the potential of sunlight. Another limitation lies in the rapid recombination of photo-generated electron-hole pairs.[24] According to time-resolved spectroscopic studies, nearly 90% of photo-induced electron-hole pairs recombine within a short time, leaving only 10% available for further reactions. This implies that merely 10% of the photoexcited charge carriers participate in the photocatalytic processes.[25] Consequently, in solar-driven applications, the photocatalytic efficiency of pure TiO_2 remains relatively low.

To address these limitations, researchers have employed various strategies to modify TiO_2 and enhance its practicality. These strategies include non-metal doping, metal doping, and dye sensitization methods. These modifications broaden the light absorption range of the samples and achieve efficient charge separation, thereby suppressing the recombination of photo-generated electron-hole pairs and achieving higher photocatalytic activity.[26] Through the doping of metals such as Pt, Au, Pd, Ru, Cu, and Ag, the photocatalytic activity of TiO_2 can be significantly enhanced.[27–32] In particular, the introduction of nano-sized Pt, Au, Ag, and other noble metal particles on the catalysts' surface can induce the surface plasmon resonance (SPR) effect, leading to oscillations of surface electrons and thus enhancing light absorption by the catalyst. This causes improved electron generation efficiency, allowing more electrons to transfer to the conduction band of TiO_2 and notably boosting the photocatalytic efficiency of the composite material. For instance, Kong et al.[33] successfully deposited Ag nanoparticles onto TiO_2 nanorods using electrochemical methods. Compared to pure TiO_2, the composite material exhibited a five-fold increase in the efficiency of photocatalytic CO_2 reduction under UV light. Similarly, Liu et al.[34] achieved a synergistic enhancement in the photocatalytic degradation and discoloration of Rhodamine B dye by co-modifying TiO_2 with carbon and Ag. Experimental results demonstrate that the composite photocatalyst exhibits significantly improved decoloration efficiency

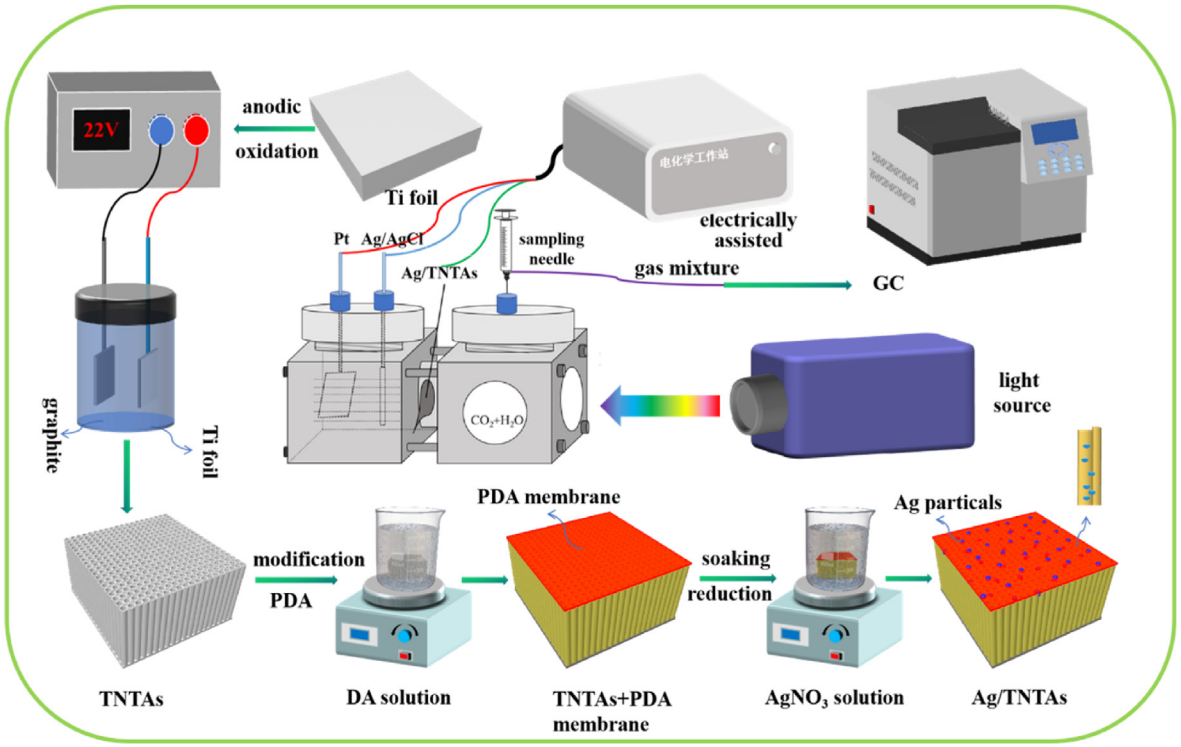

Scheme 1. Experimental process and material preparation process schematic diagram.

compared to pure TiO_2 and Ag/TiO_2.

The polydopamine (PDA) modification method involves using PDA to modify material surfaces. PDA possesses numerous functional groups, including catechol, quinone, and amine, which exhibit adhesion and versatile chemical reactivity. This property enables PDA to engage in grafting reactions effectively. Moreover, the strong hydrophilicity and mild reducibility of PDA make it a highly useful surface modifier and reaction platform.[35] For instance, Peng et al.[36] pointed out that in the process of preparing Au-coated Fe_3O_4 core-shell nanostructures, when PDA is attached to the surface of the material, the phenolic hydroxyl group carried by the retained catechol group can chelate with Au ions. During this process, catechol is oxidized to benzoquinone, forming a strong non-covalent bond with Au nanoparticles. Finally, the Au ions in the solution are reduced and fixed on the surface of the material through the groups on the PDA surface. Additionally, some of the functional groups on the PDA can adsorb metal ions in the solution and reduce them to metal elements, such as Ag and Au ions.

Inspired by the above research findings, the titanium nanotube arrays (TNTAs) with a high specific surface area, ordered arrangement, uniform pore size and excellent photocatalytic activity were fabricated using the anodic oxidation method. Additionally, Ag nanoparticles were homogeneously deposited onto the TNTAs surfaces using the PDA-modification technique. These prepared composite materials not only extend the range of light absorption but also effectively induce the SPR effect during the catalytic process, further improving the charge separation efficiency and photocatalytic activity. In this work, we employed a custom-designed H-type electro-assisted photocatalytic reaction system with dual compartments and interfaces for the photocatalytic reduction of CO_2 in ambient air. One compartment housed air with a minor water vapor content, serving as a sealed photocatalytic reactor, while another compartment contained a solid electrolyte, functioning as an electrochemical reactor. The term "dual interfaces" refers to both sides of the titanium sheet. One side forms a "nanoforest" consisting of the Ag/TNTAs composite, functioning as the light-receiving surface and the gas-solid interface in the gas-phase photocatalytic compartment, while another side acts as the working electrode and the solid-solid interface in the solid-state electrochemical compartment. In this way, the H-type catalytic reaction system integrates the gas-phase photocatalytic reaction compartment with the solid-phase electrochemical reaction compartment. It is worth noting that the designed system has its unique advantages compared with the traditional photoelectrocatalytic system. In the photocatalytic compartment, the ambient air and the catalyst can be fully contacted at the gas-solid interface, which provides more active sites for the chemical reaction, and the photocatalytic compartment does not need to add additional sacrificial agent or alkaline absorption liquid.[37] In the electrochemical compartment, the solid agar electrolyte is used instead of the liquid electrolyte, which inhibits the transmission speed of various electroactive substances, thus greatly inhibiting the occurrence of hydrogen evolution reactions. While improving the photocatalytic rate and electron utilization rate, the practical application value of the system is significantly increased. This makes it possible to realize practical applications. The specific experimental process and material preparation process are shown in Scheme 1.

2. Experimental section

2.1. Chemicals and reagents

Titanium foil (Ti, 99.99%) was purchased from Qingyuan Metal. Nitric acid (HNO_3, AR, 65%–68%), hydrofluoric acid (HF, AR, 40%) and glacial acetic acid (CH_3CO_2H, AR, 99.99%) were all purchased from Tianjin Fuyu. Sodium nitrate ($NaNO_3$, AR, 99%) was purchased from Tianjin Kemiou. The agar powder (BR) was purchased from Beijing Aoboxing. Dopamine (DA, AR, 98%) was purchased from Chengdu Huaxia. Silver nitrate ($AgNO_3$, AR, 99.8%) was purchased from China National Pharmaceutical Group. The reagents and chemicals used in the experimental procedure were directly purchased from chemical suppliers and pharmaceutical companies, and no additional purification was required. The water utilized in the experiments was self-prepared ultrapure water with a resistivity of 18.25 MΩ cm.

2.2. Syntheses

2.2.1. Synthesis of agar-based solid electrolyte

145 g $NaNO_3$ was dissolved in 150 mL water, and the saturated $NaNO_3$ solution was obtained by filtration. 11 g agar powder was added to 150 mL saturated $NaNO_3$ solution. The above solution was put into a water bath at 90 °C and stirred for 60 min to obtain a saturated $NaNO_3$ agar solution. The prepared unsolidified solution is poured into the electrolytic cell of the photocatalytic device while it is hot, and the upper cover of the device is tightened and cooled to room temperature. The prepared electrolyte is a solid gel.

2.2.2. Synthesis of TNTAs

Highly ordered and well-dispersed TNTAs were grown on Ti foil by anodic oxidation. Firstly, the Ti foil was ultrasonically cleaned in ethanol and water for 20 min, respectively. After natural drying, the Ti foil was polished and repeatedly washed with water. After natural drying, anodic oxidation was carried out at 22 V for 25 min. Ti foil was used as an anode and graphite electrode was used as a cathode. 6 mL CH_3CO_2H and 3 mL HF were added to 400 mL water as electrolytes. After the anodic oxidation, the prepared amorphous TNTAs were annealed in air at 450 °C for 3 h, and the heating rate was 5 °C min^{-1} to obtain anatase TNTAs.

2.2.3. Synthesis of Ag/TNTAs

TNTAs prepared by anodic oxidation were placed in a 50 mL DA solution with a concentration of 0.02 mol L^{-1} and shaken vigorously in a shaker for 6 h. After the reaction, the residual solution on the surface was rinsed with water and immersed in ethanol for 1 h. Then the TNTAs coated with polydopamine (PDA) were obtained by natural drying. It was placed in an $AgNO_3$ solution with a concentration of 0.2 mol L^{-1} and allowed to stand in the dark for 10 h. After the reaction, Ag/TNTAs were obtained by thoroughly washing with water and drying naturally.

2.3. Characterization

The morphological characteristics of the synthesized samples were investigated by scanning electron microscopy (SEM; JSM-7001F) equipped with an energy-dispersive X-ray spectroscopy (EDS). The internal microstructures were examined by high-resolution transmission electron microscopy (HRTEM; JEM2010). The crystal structure of the synthesized samples was analyzed by X-ray diffraction (XRD; Bruker D8 ADVANCE) with Cu Kα radiation. The optical absorption range and bandgap structure of the samples were analyzed by UV–visible diffuse reflectance spectroscopy (UV–vis DRS; UH-4150). The surface chemical composition and valence of the samples were analyzed via X-ray photoelectron spectroscopy (XPS; ESCALAB 250Xi). The photoluminescence (PL) spectra were recorded using a fluorescence spectrophotometer (FLS980, England). The impedance and photocurrent of the samples were analyzed by an electrochemical workstation (Chi660e; Shanghai Chenhua). The composition and content of photocatalytic products were analyzed by gas chromatography (GC, Shanghai Tianmei-GC-7980).

3. Results and discussion

3.1. Characterization analyses

3.1.1. XRD analyses

The X-ray diffraction pattern (Fig. 2a) clearly indicates the presence of prominent characteristic peaks at 25.3°, 37.9°, 54.1°, 62.8°, 70.5°, and 76.2°, which correspond to the crystal planes (101), (004), (105), (204), (220), and (301) of anatase TiO_2 (PDF-73-1764).[38,39] Additionally, both

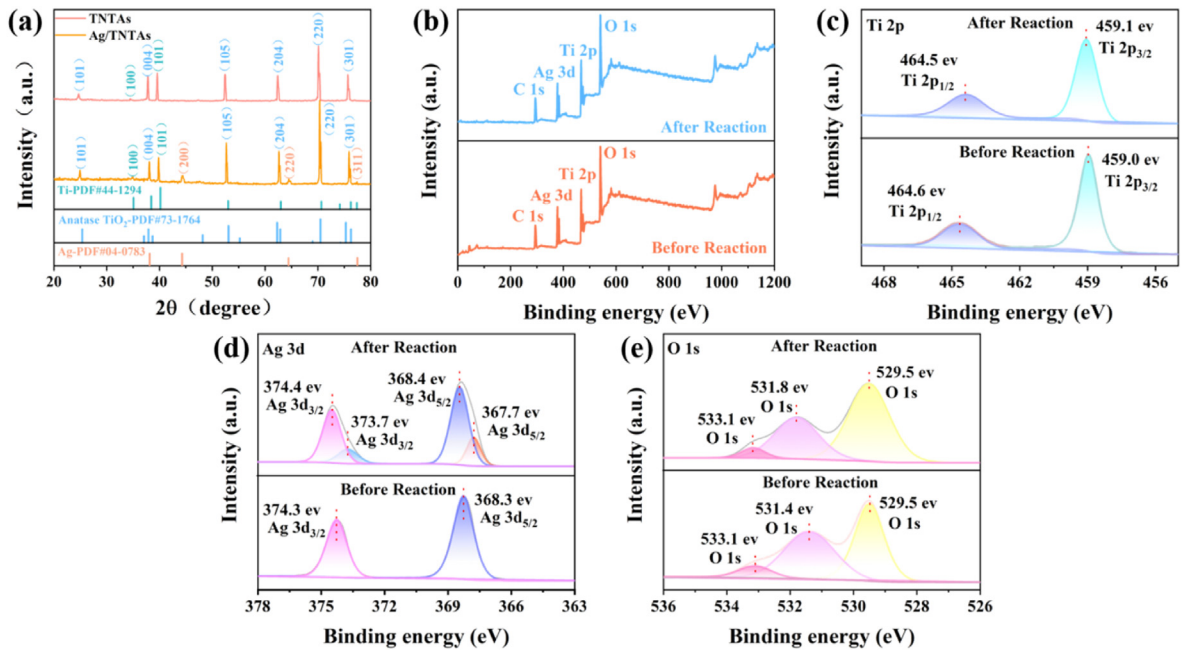

Fig. 2. (a) XRD patterns of the synthesized TNTAs and Ag/TNTAs samples. (b) XPS survey spectrum of Ag/TNTAs. (c–e) High-resolution XPS spectra of Ti 2p, Ag 3d and O 1s.

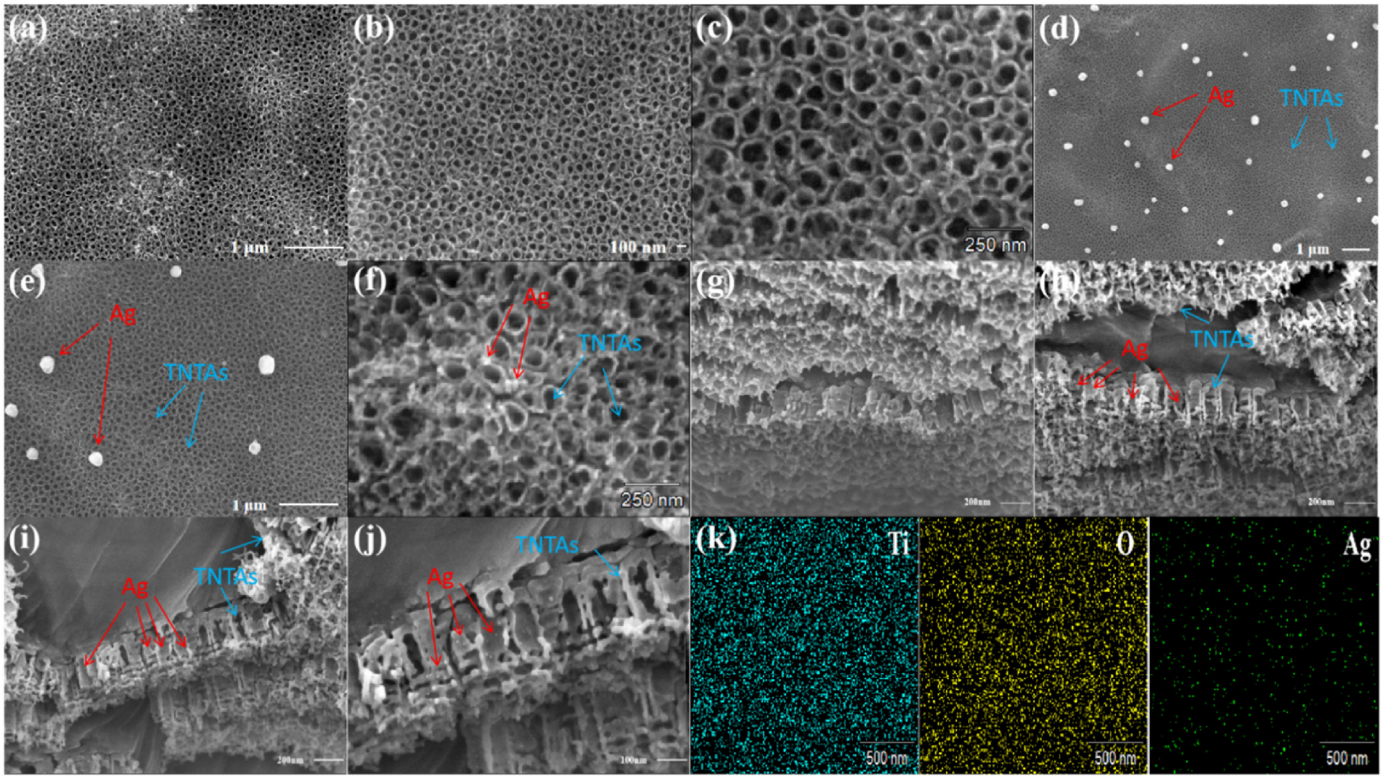

Fig. 3. SEM images of the (a–c) TNTAs and (d–f) Ag/TNTAs. (g–j) Sectional drawing of the Ag/TNTAs sample after the reaction. (k) Corresponding EDS elemental mapping of Ti, O, and Ag of Ag/TNTAs samples.

samples exhibit distinct characteristic peaks at 35.1° and 40.2°,[40] corresponding to the crystal planes (100) and (101) of Ti foil (PDF-44-1294), respectively. Moreover, due to the close position of some characteristic peaks of Ti foil and anatase TiO_2, the phenomenon of coincidence may occur. The simultaneous presence of characteristic peaks for both Ti and anatase TiO_2 can be attributed to the growth of TNTAs on a Ti foil substrate, with the reverse side of TNTAs essentially composed of Ti foil. Furthermore, the Ag/TNTAs samples exhibit additional characteristic peaks at 44.3°, 64.4°, and 77.5°, which correspond to the crystal planes (200), (220), and (311) of cubic Ag (JCPDS 04-0783),[41] respectively,

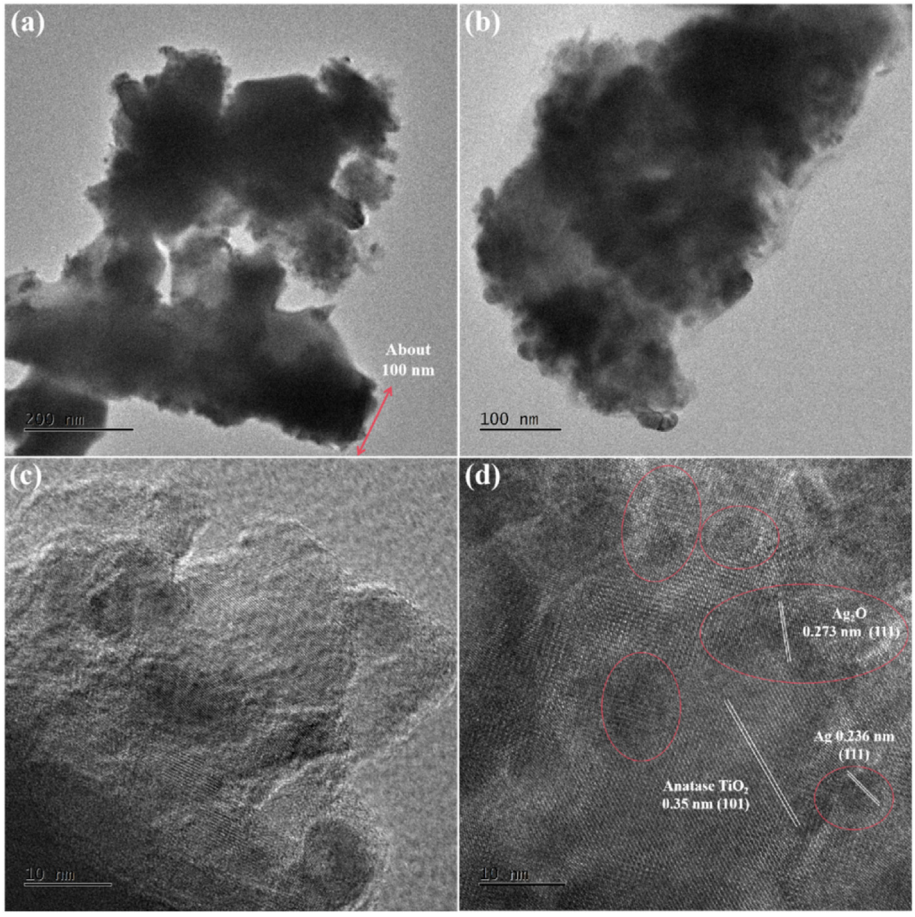

Fig. 4. (a, b) Low resolution TEM images of the Ag/TNTAs. (c, d) High resolution TEM images of the Ag/TNTAs.

indicating the successful loading of Ag particles onto TNTAs. The low diffraction intensity can be attributed to the small amount of Ag particles loaded.

3.1.2. XPS analyses

XPS analysis was conducted to investigate the chemical composition, valence state distribution, and electron transfer pathways of the Ag/TNTAs samples. The full XPS survey spectrum (Fig. 2b) clearly shows the main peaks corresponding to each element present in the Ag/TNTAs composite material, confirming its composition of Ti, O, and Ag. There was no significant change in the total spectrum before and after the reaction, indicating that the composite material remained stable during the catalytic reaction. The Ti 2p XPS spectrum (Fig. 2c) before the reaction exhibits two peaks located at binding energies of 464.6 and 459.0 eV, which conform to Ti $2p_{1/2}$ and Ti $2p_{3/2}$, respectively. And the Ti 2p XPS spectrum after the reaction has almost no deviation. This implies that Ti exists in the form of Ti^{4+} before and after the reaction.[42,43] The Ag 3d XPS spectrum (Fig. 2d) before the reaction displays two main peaks at binding energies of 374.3 and 368.3 eV, which correspond to Ag $3d_{3/2}$ and Ag $3d_{5/2}$ of elemental Ag. The Ag 3d XPS spectrum after the reaction found two additional peaks at 373.7 and 367.7 eV, respectively, corresponding to Ag $3d_{3/2}$ and Ag $3d_{5/2}$ of Ag^{+}.[44,45] This result reveals that some Ag particles were oxidized to Ag_2O on the surface of the sample after the reaction, while the other Ag particles were not oxidized due to the protection of the PDA layer. At this time, the sample was in the coexistence state of Ag and Ag^{+}. The O 1s XPS spectrum (Fig. 2e) before the reaction exhibits three distinct peaks at binding energies of 533.1, 531.4, and 529.5 eV, corresponding to adsorbed oxygen (O–H–O), surface oxygen and lattice oxygen, respectively.[45] These three different forms of oxygen establish the presence of O^{2-}, OH^{-}, and H_2O molecules and oxygen vacancies on the surface of the sample. The O 1s XPS spectrum after the reaction reflects that the lattice oxygen increases slightly and the surface oxygen decreases slightly. This may be because some Ag particles on the surface of the sample are oxidized to Ag_2O, which reduces the oxygen vacancies. At the same time, Ag combines with O to form additional lattice oxygen, which is consistent with the above conclusions. Moreover, a slight shift in the XPS spectrum suggests an electronic interaction within the composite molecule. This confirms the successful loading of Ag particles onto TNTAs through PDA modification, and during the photocatalytic reaction, a part of Ag particles are oxidized to Ag_2O, forming a tight heterostructure.

3.1.3. SEM and EDS analyses

The microstructure and morphology of TNTAs and Ag/TNTAs samples were observed by SEM. The layered and ordered structure of TNTAs can be clearly observed (Fig. 3a–c). The TNTAs exhibit a large specific surface area, uniform arrangement, uniform pore size, and a diameter of approximately 100 nm after anodization. Fig. 3d–f shows the morphology of Ag/TNTAs modified by PDA under SEM. In the low-magnification SEM images (Fig. 3d–e), apart from the tubular array structure of TNTAs, particles with a diameter of about 100–300 nm can also be observed. The result may be caused by the agglomeration of a small number of Ag nanoparticles during the reduction of Ag nanoparticles by PDA. The high-magnification SEM image (Fig. 3f) reveals that the loaded Ag particles are uniformly attached to the wall of the TNTAs surface on the mesh PDA layer. In addition, due to the small size of some silver particles, they may enter the interior of the tubular structure. We observed the sectional drawing of the Ag/TNTAs sample after the reaction (Fig. 3g–j) by the secondary electron method. The sectional drawing also shows the neat arrangement of the sample. At the

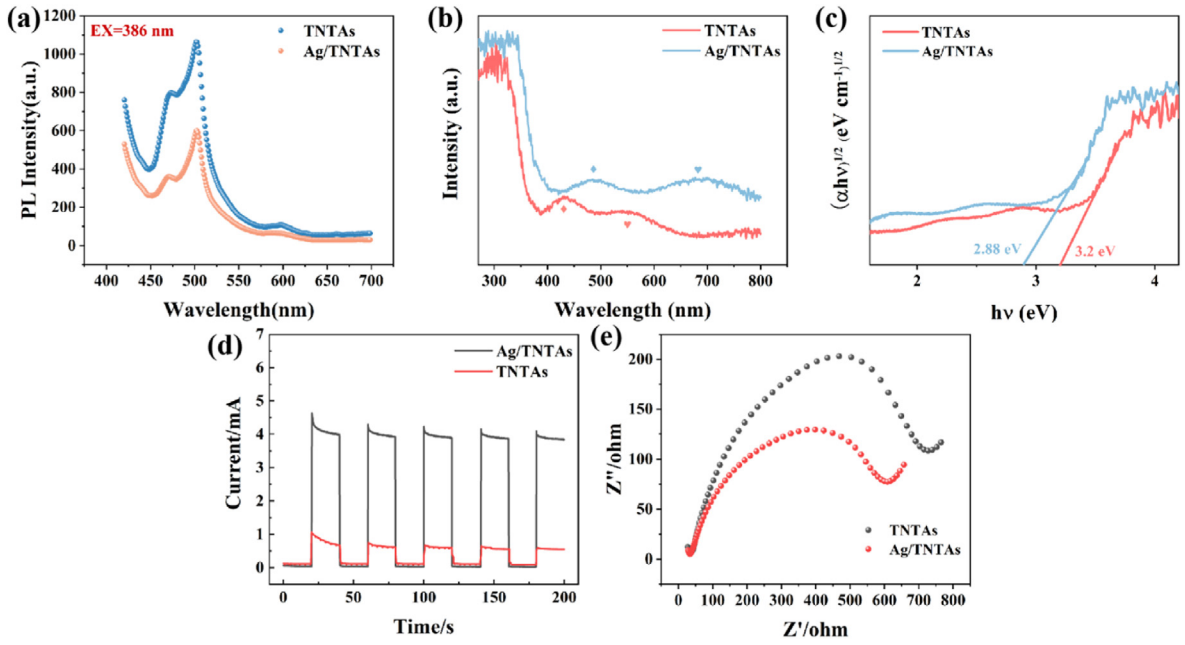

Fig. 5. Experimental comparison of TNTAs and Ag/TNTAs samples. (a) PL spectra (excitation wavelength at 386 nm). (b) UV–Vis diffuse reflectance spectra. (c) Plots of $(\alpha h\nu)^{1/2}$ against the photon energy. (d) Photocurrent response diagram. (e) EIS curves.

same time, we can perceive the uniform distribution of Ag nanoparticles inside the TNTAs tube through the high-power diagram. During the catalytic reaction, Ag/TNTAs sample can cause surface electron oscillation, produce an SPR effect, and improve the photocatalytic activity. The corresponding EDS spectra (Fig. 3k and Figs. S1–2), full scale counts (Figs. S3–4) and quantitative results (Figs. S5–6) showed the element distribution of TNTAs and Ag/TNTAs composites. Except for a small amount of Ag particles agglomerated, all elements were uniformly distributed in the samples.

3.1.4. TEM analyses

The mixture of TNTAs, Ag and Ag_2O gathered on the surface of the sample was scraped and ultrasonically shocked, and its lattice structure and exposed crystal plane were characterized by TEM. In the low resolution TEM image (Fig. 4a–b), aggregated Ag/Ag_2O particles and similar tubular TNTAs can be observed. Scratching and ultrasonic oscillation may lead to a certain degree of deformation of TNTAs, but the diameter of the tube is consistent with the SEM image. In the high resolution TEM image (Fig. 4c–d), the lattice fringe width of Ag particles, Ag_2O particles, and TNTAs are 0.236, 0.273, and 0.351 nm, corresponding to their respective (111), (111), and (101) crystal planes. The results show that some Ag particles on the surface of TNTAs are oxidized to Ag_2O during the reaction, which is in line with the above characterization results. In addition, the element distribution was characterized by EDS equipped with high resolution TEM, and the results agreed with the above discussion (Fig. S7).

3.1.5. PL analyses

The PL spectra were analyzed to understand the migration of photogenerated carriers. Fig. 5a shows that both TNTAs and Ag/TNTAs exhibit three significant peaks in the wavelength range of 450–650 nm when excited at a wavelength of 386 nm. The PL spectrum of the original TNTAs exhibits the strongest peak intensity due to its fast photogenerated carrier recombination rate. However, with the loading of Ag nanoparticles, the fluorescence of Ag/TNTAs is effectively quenched, and the peak intensity of the PL spectrum is significantly reduced. This indicates that the recombination of photogenerated carriers and photocorrosion are effectively inhibited after loading Ag nanoparticles, demonstrating excellent charge separation and migration ability.

3.1.6. UV–vis analyses

UV–Vis diffuse reflectance spectroscopy was used to characterize the optical absorption properties and optical band gap of pure TNTAs and Ag/TNTAs composites. The original TNTAs exhibit a light absorption edge at 384 nm. However, when Ag particles are loaded into TNTAs, the light absorption range increases and the absorption edge expands to 435 nm (Fig. 5b). This establishes that TNTAs have almost no response in the visible light range, while Ag/TNTAs show a red shift in visible light absorption and an increase in absorption intensity, thereby improving the overall photocatalytic activity. According to the relationship between the energy band gap (E_g) and incident photon energy ($h\nu$) :

$$\alpha h\nu = K(h\nu - E_g)^n \quad (1)$$

where α is the absorption coefficient and K is the absorption constant. By plotting the ratio of $(\alpha h\nu)^{1/2}$ to $h\nu$ (Fig. 5c), it is determined that the E_g of TNTAs and Ag/TNTAs are 3.2 and 2.88 eV, respectively. This shows that the introduction of Ag nanoparticles can broaden the light response range of TNTAs, allowing them to exhibit good photocatalytic activity in the visible light range.

3.2. Electrochemical analysis

3.2.1. Photocurrent analysis

To investigate the interfacial charge separation efficiency and photoelectrochemical response ability of the samples, the photocurrent responses of TNTAs and Ag/TNTAs samples were tested using a three-electrode system in 0.1 mol L^{-1} $NaNO_3$ electrolyte solution with visible light as a light source and bias voltage of 0.3 V (vs. Ag/AgCl, the same as below). The system consisted of a platinum electrode, an Ag/AgCl reference electrode, and a working electrode. The Ag/TNTAs sample exhibits a stronger photocurrent compared to TNTAs (Fig. 5d). This enhancement can be attributed to the presence of Ag nanoparticles, which introduce defects on the surface of TNTAs, leading to increased light response intensity. Additionally, some small Ag nanoparticles may infiltrate the interior of TNTAs, causing the SPR effect. This effect leads to oscillation under light, significantly improving the light response ability and catalytic performance of the samples. Furthermore, the oxidation ability of the photogenerated holes plays a significant role. During the photocatalytic reaction, the Ag nanoparticles on the surface of the

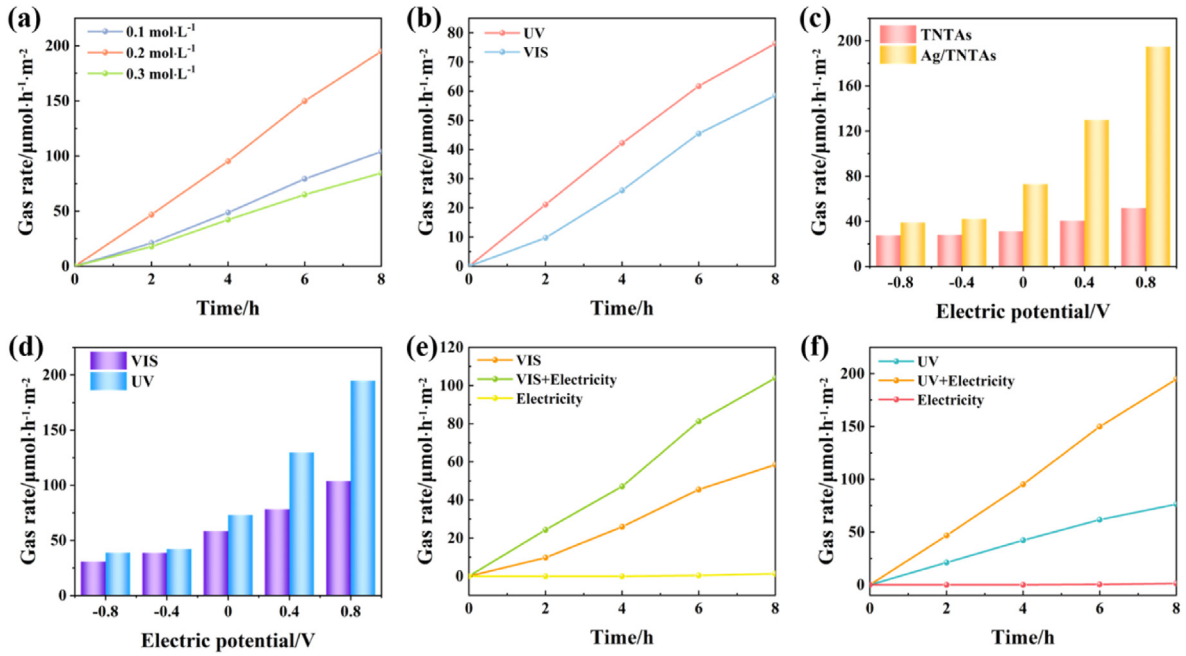

Fig. 6. (a) Diagram of the effect of different Ag loadings on CO formation rate. (b) CO formation rate diagram under UV and visible light sources. (c, d) Diagram of the effect of different applied potentials on the CO formation rate under UV and visible light sources. (e, f) Analysis diagram of photoelectric coupling effect under UV and visible light sources.

samples may be oxidized to Ag_2O, forming a heterojunction with TNTAs. As a result, photogenerated electrons from the conduction band (CB) of Ag_2O move to the CB of TNTAs, while the holes on the valence band (VB) of TNTAs move to the VB of Ag_2O. This effective separation of photogenerated electrons and holes contributes to a higher photocurrent density. Moreover, the close contact between the P–N heterostructure formed by TNTAs and Ag_2O also promotes charge transfer at the interface, which improves charge separation efficiency, and electron lifetime, and enhances the photocatalytic activity.

3.2.2. EIS analysis

EIS is commonly used to characterize charge carrier transport and provides additional evidence for the above results. The Ag/TNTAs sample exhibits a smaller semicircle diameter compared to the original TNTAs sample (Fig. 5e), indicating substantially reduced charge transport impedance at the Ag/TNTAs interface, thereby enhancing the separation and migration of photogenerated electrons and holes. This effect can be ascribed to the excellent electrical conductivity of Ag-loaded nanoparticles, which establishes a more efficient electron transport pathway, mitigating charge accumulation and transmission. Furthermore, Ag nanoparticles inside TNTAs induce the SPR effect, prompting surface electron oscillations, thereby increasing electron mobility and playing an important role in augmenting photocatalytic activity.

3.3. Performance analysis of photocatalytic reduction of CO_2

3.3.1. Effect of Ag nanoparticle loading on photocatalytic activity

To investigate the impact of Ag nanoparticle loading on the photocatalytic activity of the composites, TNTAs with PDA adhesion layer were immersed in different concentrations of $AgNO_3$ solution to obtain Ag/TNTAs samples with different Ag nanoparticle loadings, and the photocatalytic reduction experiments of CO_2 were performed. The photocatalytic performance of Ag/TNTAs samples exhibited enhancement with the introduction of Ag nanoparticles (Fig. 6a). Notably, the Ag/TNTAs sample produced via PDA modification in an $AgNO_3$ solution with a concentration of 0.2 mol L^{-1} demonstrated the best photocatalytic performance. This is because when the loading amount of Ag nanoparticles is too low, the photocatalytic performance improvement rate of the sample is low; conversely, the sample matrix will be blocked, hindering its response to light and utilization.

3.3.2. Photocatalytic CO_2 reduction activity

The prepared TNTAs and Ag/TNTAs samples were placed in a custom-designed H-type photocatalytic reaction system for CO_2 reduction in ambient air. Gas reduction products were subsequently analyzed and detected by gas chromatograph. When UV light served as the light source (Fig. 6b), the catalytic reaction yielded 76.33 μmol h^{-1} m^{-2} of CO after 8 h. In theory, the conversion rate of atmospheric CO_2 under UV light can reach 12%. Conversely, when visible light was employed as the light source, the catalytic reaction yielded 58.46 μmol h^{-1} m^{-2} of CO for 8 h. In theory, the conversion rate of atmospheric CO_2 under visible light can reach 9%. The photocatalytic activity of TNTAs is evidently superior under UV light because the TNTAs substrate of the composite material exclusively responds to UV light and remains unresponsive to visible light. Additionally, UV light possesses higher energy levels than visible light, rendering it more conducive to excitation. Clearly, the incorporation of Ag nanoparticles can enhance the material's responsiveness to UV light while broadening its spectral sensitivity to visible light. Furthermore, regardless of whether UV or visible light is employed, the Ag/TNTAs composite demonstrates an effective reduction of low-concentration atmospheric CO_2 in ambient air into CO, underscoring its favorable selectivity for CO production.

3.3.3. Effect of applied potentials on the photocatalytic reduction of CO_2

The experimental setup involved maintaining consistent conditions for the photocatalytic reduction of CO_2 in ambient air while varying the applied potentials using an electrochemical workstation. The resulting CO production at different applied potentials was analyzed and quantified by gas chromatography, so as to analyze the effect of different applied potentials on the photocatalytic reduction of CO_2. The results (Fig. 6c–d) indicate a positive correlation between the yield of photocatalytic product CO and the applied potential, regardless of whether UV or visible light was used as the light source. Clearly, the yield of CO was significantly higher at positive potentials compared to negative

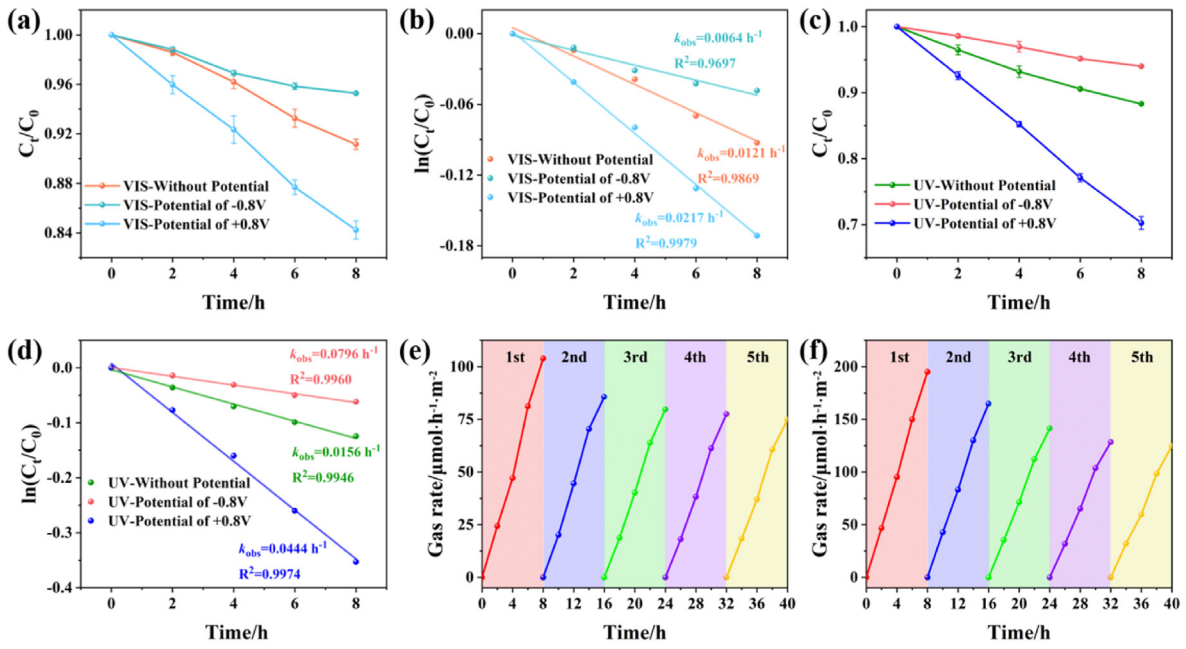

Fig. 7. (a, c) Diagram of CO_2 conversion in different potentials within 8 h under UV and visible light sources. (b, d) Kinetic analysis diagram of CO_2 conversion within 8 h under UV and visible light sources. (e, f) Diagram of catalyst stability in 5 reaction cycles under UV and visible light sources.

potentials, with the highest yield observed at +0.8 V. Specifically, after 8 h of UV light catalysis, the yield of CO reached 194.9 μmol h^{-1} m^{-2}, corresponding to a theoretical conversion rate of 30% for CO_2 in ambient air. Similarly, after 8 h of visible light catalysis, the yield of CO was 103.9 μmol h^{-1} m^{-2}, resulting in a theoretical conversion rate of 16% for CO_2 in ambient air. These values were notably higher than those obtained without potential assistance. This enhancement can be attributed to the utilization of agar solid electrolytes in our electrochemical reaction system. Although the reaction rate on the working electrode was rapid within the range of −0.8 V to +0.8 V, the migration and diffusion of the electroactive substance in the agar were very slow, resulting in a weak current in the external circuit. Consequently, the migration of photogenerated electrons to the counter electrode through the external circuit was hindered, effectively suppressing the side reaction of H_2 on the surface of the counter electrode capturing electrons in the electrochemical reaction compartment. Under UV or visible light irradiation, the catalyst generated photogenerated electrons and holes. Photogenerated holes oxidized a portion of Ag nanoparticles on the surface of TNTAs, forming a P–N heterostructure with TNTAs and Ag_2O. At this point, the external electric field generated by applying a positive potential aligned with the internal electric field direction of the TNTAs/Ag_2O heterojunction, facilitating the migration and aggregation of

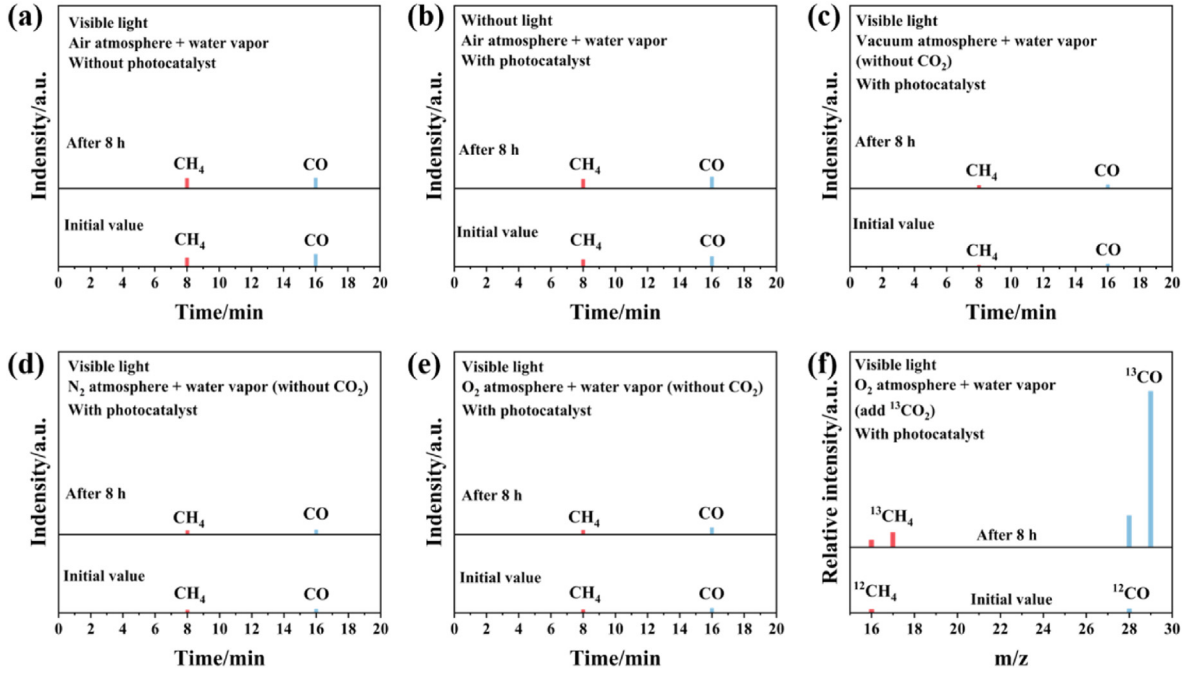

Fig. 8. (a–e) GC results of control experiments (1-5). (f) GC-MS results of control experiments (6).

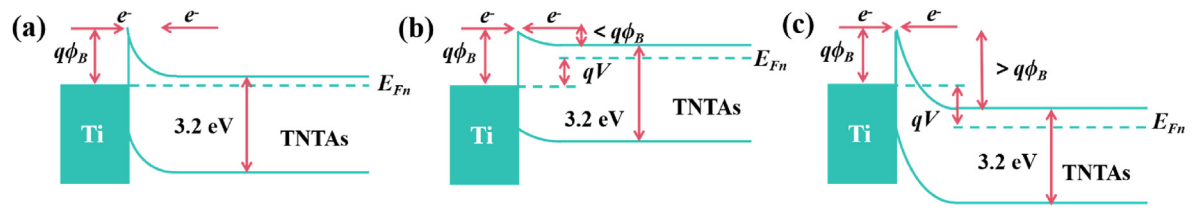

Fig. 9. Schematic diagram of Ti/TNTAs Schottky barrier change without extra potential (a), with extra positive potential (b), and with extra negative potential (c).

photogenerated electrons from the CB of Ag_2O to the CB of TNTAs. Simultaneously, photogenerated holes from the VB of TNTAs migrated and aggregated to the VB of Ag_2O, effectively promoting the separation of photogenerated electrons and holes. Furthermore, this process triggered the SPR effect of Ag nanoparticles inside the TNTAs, thereby improving the catalytic performance of the composites and consequently increasing the yield of CO.

3.3.4. *Effect of photoelectric coupling*

In order to verify the photoelectric coupling effect in the electro-assisted photocatalytic reaction system, the Ag/TNTAs samples were tested for photocatalytic reduction of CO_2 in ambient air under UV light and visible light. Specifically (Fig. 6e–f), the Ag/TNTAs samples exhibited excellent catalytic effects on CO_2 in ambient air, irrespective of the light source used. However, when only a +0.8 V potential was applied, there was minimal catalytic effect on CO_2 in ambient air. Furthermore, the yield of the photocatalytic reduction product CO was significantly enhanced with the assistance of the +0.8 V potential. The combination of these results, along with the yield of CO under different applied potentials, provides evidence for the existence of a photoelectric coupling effect in the catalytic process.

3.3.5. *Kinetic model and repeatability*

To investigate the reduction of CO_2 during an 8 h catalytic process, 400 ppm of CO_2 in ambient air was used as the initial carbon source. The amount of CO produced in the reduction process served as a representation, and a kinetic model was fitted to the data. The results demonstrated that the photocatalytic process alone, as well as the ±0.8 V potential-assisted photocatalytic processes, all followed a first-order kinetic model with a high degree of fitting (Fig. 7a–d). By examining the k values, the distinct reaction rates among the three processes can be observed clearly that the +0.8 V potential-assisted photocatalysis exhibited the highest rate, followed by single photocatalysis, and finally the −0.8 V potential-assisted photocatalysis. These findings align with the previous results and suggest that the CO_2 reduction pathway in this catalytic process is straightforward, involving fewer intermediates and reaction steps. Additionally, the model indicates that the catalyst prepared possesses high surface activity, enabling effective adsorption and catalysis the reduction of CO_2 to produce CO under the specified conditions. Furthermore, the active sites of the catalyst remain stable, allowing for continuous catalytic reduction of CO_2 in ambient air. To assess the repeatability of the catalyst, the tests under both UV and visible light were conducted (Fig. 7e–f). Using an 8 h cycle, we found that the yield of CO reached 64% and 72% of the first cycle after 5 cycles. Although the photocatalytic performance of Ag/TNTAs decreased due to photocorrosion, no further decrease was observed after 5 cycles of experiments. This shows that the composite material has a certain repeatability.

3.3.6. *Carbon source verification*

In order to prove that photocatalytic products are converted from CO_2 in ambient air, we referred to the literature and designed 6 sets of controlled experiments,[46,47] and the electro-assisted photocatalytic products after 8 h were detected by GC and GC-MS. (1) Visible light, air atmosphere + water vapor, without photocatalyst. Almost no photocatalytic products were detected (Fig. 8a), which proved that the photocatalytic reaction was induced by the catalyst; (2) Without light, air atmosphere + water vapor, with photocatalyst. Almost no photocatalytic products were detected (Fig. 8b), which proved that the photocatalytic reaction was induced by light; (3) Visible light, vacuum atmosphere + water vapor (without CO_2), with photocatalyst; (4) Visible light, N_2 atmosphere + water vapor (without CO_2), with photocatalyst; (5) Visible light, O_2 atmosphere + water vapor (without CO_2), with photocatalyst. The photocatalytic products were almost not detected (Fig. 8c-e) in the control experiments (3-5), which proved that the carbon source did not come from other components such as materials, and other components in the ambient air did not directly participate in the photocatalytic reaction. (6) On the basis of the control experiment (5), $^{13}CO_2$ was obtained by the reaction of ^{13}C-labeled $NaH^{13}CO_3$ with H_2SO_4, and a certain amount of $^{13}CO_2$ was injected into the reactor for electro-assisted photocatalytic reaction. GC-MS detection showed that most of the photocatalytic products were labeled with ^{13}C (Fig. 8f). The above control experiments show that the source of photocatalytic products is CO_2 in the environment.

3.4. *Possible mechanism of charge transfer*

3.4.1. *Mechanism of charge transfer in Ti/TNTAs sample*

Based on the above characterization results and experimental data, the potential transfer pathway of carriers in the photocatalytic reduction of CO_2 in ambient air using TNTAs and Ag/TNTAs samples was investigated. Fig. 9 shows the schematic diagram of the Schottky barrier change of TNTAs after the application of a certain potential. Here, q_B represents the work function, E_F stands for the Fermi level, qV represents the energy provided by the potential, and E_{Fn} denotes the Fermi level after displacement. As mentioned above, TNTAs are formed through the anodic oxidation of Ti foil, with one side (i.e. light-receiving surface) oxidized to TNTAs and another side remaining as a Ti sheet. In this configuration, it can be considered a composite material composed of TNTAs and Ti. When the two materials come into contact, the different Fermi levels result in electron diffusion from the conduction band of the semiconductor TNTAs to the Ti sheet until both sides of the contact surface reach an equilibrium state (Fig. 9a). Consequently, the energy band of the semiconductor TNTAs bends due to the internal electric field, forming a Schottky barrier on the contact surface. Applying a potential to Ti/TNTAs through an external electric field affects the Fermi level on the TNTAs side, leading to a change in the Schottky barrier between the two materials. When a positive potential is applied (Fig. 9b), the Fermi level on the TNTAs side increases, reducing the height of the Schottky barrier. This facilitates the transfer of electrons from the CB of TNTAs to the contact surface of the Ti sheet. Although these electrons will be bound to the Ti sheet, the presence of the Schottky barrier effectively promotes the separation of electron-hole pairs, thereby enhancing catalytic efficiency. Conversely, applying a negative potential increases the Schottky barrier height (Fig. 9c), making it more difficult for electrons in the CB of TNTAs to transfer to the Ti sheet. This result thus enhances the recombination rate of electron-hole pairs and reduces catalytic efficiency.

3.4.2. *Possible mechanism of the catalytic reaction of Ag/TNTAs*

On the basis of the above reaction mechanism, we analyze the

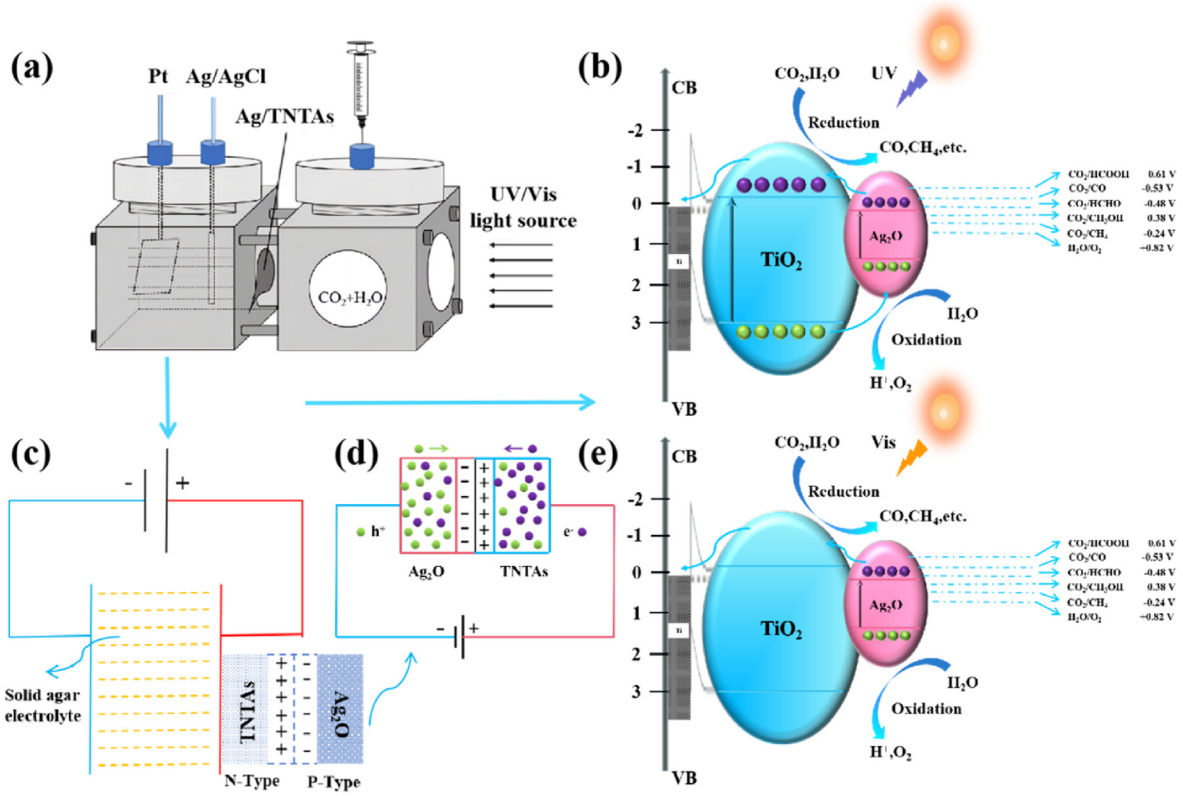

Fig. 10. Possible catalytic reaction mechanism diagram. (a) H-type electro-assisted photocatalytic reaction device. (b, e) Transfer path of charge carriers in the process of UV and visible light photocatalysis. (c) Potential-assisted mechanism diagram. (d) P–N heterojunction simple diagram.

potential reaction mechanism of the P–N heterojunction. During the photocatalytic reaction process, a portion of the Ag nanoparticles undergo a transformation into P-type semiconductor Ag_2O due to the combined effects of oxygen, photogenerated holes and positive potential. This results in the formation of a P–N heterojunction with the N-type semiconductor TNTAs (Fig. 10d). The remaining Ag nanoparticles serve to introduce additional defects on the surface of TNTAs, while also inducing the SPR effect inside the TNTAs to enhance photocatalytic efficiency. In the absence of light, electrons and holes in the P–N heterojunction diffuse freely, establishing an internal electric field and reaching an equilibrium state. Under the condition of UV light catalysis (Fig. 10b), TNTAs and Ag_2O can be excited, generating a large number of photogenerated electrons and holes. However, due to the potential barriers, only the photogenerated electrons from Ag_2O and the photogenerated holes from TNTAs are able to drift through the junction under the influence of the internal electric field when they approach the junction electric field. The photogenerated electrons are drawn to the CB of TNTAs, while the electrons on the CB of TNTAs diffuse to the Ti sheet due to the difference in Fermi energy levels. This process continues until a Schottky barrier is formed, impeding further electron diffusion. Simultaneously, the photogenerated holes are drawn to the VB of Ag_2O. This process generates a photogenerated electric field that opposes the direction of the internal electric field within the thermally balanced P–N heterojunction, ultimately achieving equilibrium. This process effectively separates the photogenerated electron-hole pairs, leading to improved photocatalytic efficiency. The application of an external electric field not only alters the Fermi level of the semiconductor but also affects the transfer of photogenerated electrons and holes. When a positive potential is applied to TNTAs, the direction of the external electric field is consistent with the direction of the internal electric field current. Consequently, more electrons are drawn to the CB of TNTAs, while the positive potential elevates the Fermi level of TNTAs and reduces the Schottky barrier between TNTAs and Ti sheets. As a result, a small amount of electrons diffuse back to the Ti side. Furthermore, more holes are drawn to the VB of Ag_2O, further facilitating the effective separation of electron-hole pairs and enhancing the photocatalytic efficiency. Conversely, when a negative potential is applied to TNTAs, the external electric field opposes the internal electric field current, weakening the built-in electric field. Additionally, the negative potential lowers the Fermi level of TNTAs, impeding the migration of electron-hole pairs and reducing photocatalytic efficiency. Similarly, under the condition of visible light catalysis (Fig. 10e), only Ag_2O is excited to generate photogenerated electrons and holes. TNTAs, in this case, primarily serve as carriers for electron transfer. The photogenerated electrons from Ag_2O migrate to the CB of TNTAs under the influence of the internal electric field, achieving the separation of photogenerated electrons and holes and improving the photocatalytic efficiency. However, due to the lower energy of visible light compared to that of UV light, and the limited excitation of TNTAs, the number of photogenerated electrons and holes is reduced, resulting in lower catalytic effects under visible light. When an external potential is applied to assist catalysis, the conclusion is consistent with the above observations.

An H-type electro-assisted photocatalytic reaction system with dual compartments and interfaces (Fig. 10a) was used in the study. Prior to illumination, a specific potential range (−0.8V–+0.8V) was applied to the photocatalytic composite material. Due to the implementation of a solid electrolyte in the system, the external circuit exhibited a weak current, and there was minimal redox reaction occurring on the surface of both the working electrode (composite material) and the counter electrode (Pt sheet). Upon exposure to light of a specific wavelength, a significant number of photogenerated electrons and holes were generated on the surface of the photocatalyst. While some electrons were drawn to the external circuit, the slow migration and diffusion rate of the electroactive substances (Na^+, H^+, OH^-, NO^{3-}, etc.) in the solid electrolyte resulted in only a min fraction of the electrons migrating to the counter electrode, thereby inhibiting the hydrogen evolution reaction. At this

stage, the electrochemical compartment can be regarded as a capacitor-like structure, impeding electron migration (Fig. 10c). When a positive potential was applied, the current direction of the external circuit aligned with the electric field direction in the P–N heterojunction, facilitating the separation of electron-hole pairs and enhancing the photocatalytic efficiency. Conversely, a negative potential reversed the current direction in the external circuit, opposing the electric field in the P–N heterojunction and hindering the separation of electron-hole pairs, and thus reducing photocatalytic efficiency. Additionally, the majority of photocatalytic products observed in this study were CO. This can be explained by the higher thermodynamic energy required to convert CO_2 into CO compared to CH_4, CH_3OH, and HCHO. However, since only two electrons need to be transferred in the actual reaction, the kinetics of CO conversion are more favorable. Consequently, when the CB energy of electrons is sufficient to support the conversion of CO_2 into CO, CO becomes the primary reaction product.

4. Conclusion

In general, compared to pure TNTAs, the Ag/TNTAs composites prepared using the PDA modification method exhibit superior photocatalytic reduction effect on CO_2 in ambient air under UV and visible light irradiation. The incorporation of Ag nanoparticles expands the light response range of TNTAs, enabling excellent photocatalytic activity even under visible light irradiation. The excellent catalytic effect is mainly attributed to the formation of P–N heterojunction during the catalytic process and the SPR effect. In addition, the constructed electro-assisted photocatalytic system not only proves the photoelectric coupling effect but also realizes the stable, efficient and highly selective conversion of CO_2 to CO in ambient air on the gas-solid interface without sacrificial agent and alkali absorption solution. Furthermore, the catalyst has good stability, and the photocatalytic products exhibit excellent selectivity towards CO. This study is helpful in developing the practical application of photocatalytic technology and provides new insights and data support for the realization of the carbon cycle.

Declaration of competing interest

There is no conflict of interest to declare.

Acknowledgements

This research did not receive any specific grant from funding agencies in the public, commercial, or not-for-profit sectors.

Appendix A. Supplementary data

Supplementary data to this article can be found online at https://doi.org/10.1016/j.matre.2024.100269.

References

1. Qu T, Wei S, Xiong Z, Zhang J, Zhao Y. Progress and prospect of CO_2 photocatalytic reduction to methanol. *Fuel Process Technol.* 2023;251:107933.
2. Wang W, Wang L, Su W, Xing Y. Photocatalytic CO_2 reduction over copper-based materials: a review. *J CO2 Util.* 2022;61:102056.
3. Xie F, Chen R, Zhu X, et al. CO_2 utilization: direct power generation by a coupled system that integrates photocatalytic reduction of CO_2 with photocatalytic fuel cell. *J CO2 Util.* 2019;32:31–36.
4. Zhai R, Zhang L, Gu M, et al. A review of phosphorus structures as CO_2 reduction photocatalysts. *Small.* 2023;19(19):e2207840.
5. Zhu X, Ji H, Yi J, et al. A specifically exposed cobalt oxide/carbon nitride 2D heterostructure for carbon dioxide photoreduction. *Ind Eng Chem Res.* 2018;57:17394–17400.
6. Liu X, Chen T, Xue Y, et al. Nanoarchitectonics of MXene/semiconductor heterojunctions toward artificial photosynthesis via photocatalytic CO_2 reduction. *Coord Chem Rev.* 2022;459:214440.
7. Zhang H, Li MM-J. Crafting an active center with a local charge density gradient to facilitate photocatalytic ethylene production from CO_2. *Curr Opin Green Sustainable Chem.* 2022;36:100646.
8. Li D, Kassymova M, Cai X, Zang S-Q, Jiang H-L. Photocatalytic CO_2 reduction over metal-organic framework-based materials. *Coord Chem Rev.* 2020;412:213262.
9. Fu H, Liu X, Wu Y, et al. Construction of a bismuth-based perovskite direct Z-scheme heterojunction Au-$Cs_3Bi_2Br_9/V_2O_5$ for efficient photocatalytic CO_2 reduction. *Appl Surf Sci.* 2023;622(1):156964.
10. Shang Z, Feng X, Chen G, Qin R, Han Y. Recent advances on single-atom catalysts for photocatalytic CO_2 reduction. *Small.* 2023. https://doi.org/10.1002/smll.202304975.
11. Guo Rt, Wang J, Bi Zx, Chen X, Hu X, Pan Wg. Recent advances and perspectives of core-shell nanostructured materials for photocatalytic CO_2 reduction. *Small.* 2023;19(9):e2206314.
12. Rehman ZU, Bilal M, Hou J, et al. Photocatalytic CO_2 reduction using TiO_2-based photocatalysts and TiO_2 Z-scheme heterojunction composites: a review. *Molecules.* 2022;27(7):2069.
13. Wang J, Guo R-t, Bi Z-x, Chen X, Hu X, Pan W-g. A review on TiO_{2-x}-based materials for photocatalytic CO_2 reduction. *Nanoscale.* 2022;14:11512–11528.
14. Gotico P, Del Vecchio A, Audisio D, et al. Visible-light-driven reduction of CO_2 to CO and its subsequent valorization in carbonylation chemistry and ^{13}C isotope labeling. *ChemPhotoChem.* 2018;2:715–719.
15. Shi L, Zhou Z, Zhang Y, Ling C, Li Q, Wang J. Photocatalytic conversion of CO to fuels with water by B-doped graphene/g-C_3N_4 heterostructure. *Sci Bull.* 2021;66:1186–1193.
16. Chen Z, Zhao J, Zhao J, Chen Z, Yin L. Frustrated Lewis pairs photocatalyst for visible light-driven reduction of CO to multi-carbon chemicals. *Nanoscale.* 2019;11:20777–20784.
17. Dong W-W, Jia J, Wang Y, et al. Visible-light-driven solvent-free photocatalytic CO_2 reduction to CO by Co-MOF/Cu_2O heterojunction with superior selectivity. *Chem Eng J.* 2022;438:135622.
18. Wang J, Hu C, Zhang Y, Huang H. Engineering piezoelectricity and strain sensitivity in CdS to promote piezocatalytic hydrogen evolution. *Chin J Catal.* 2022;43:1277–1285.
19. Yang M-M, Cao J-M, Qi G-D, et al. Construction of low-cost Z-scheme heterojunction Cu_2O/PCN-250 photocatalysts simultaneously for the enhanced photoreduction of CO_2 to alcohols and photooxidation of water. *Inorg Chem.* 2023;62:15963–15970.
20. Hammad A, Anzai A, Zhu X, et al. Photodeposition conditions of silver cocatalyst on titanium oxide photocatalyst directing product selectivity in photocatalytic reduction of carbon dioxide with water. *Catal Lett.* 2019;150:1081–1088.
21. Li M, Qiu J, Yang L, Feng Y, Yao J. Fabrication of TiO_2 embedded $ZnIn_2S_4$ nanosheets for efficient Cr(VI) reduction. *Mater Res Bull.* 2020;122:110671.
22. Ku Y, Huang Y-H, Chou Y-C. Preparation and characterization of ZnO/TiO_2 for the photocatalytic reduction of Cr(VI) in aqueous solution. *J Mol Catal Chem.* 2011;342–343:18–22.
23. Ji D-l, Zhu J, Ji M, Leng Y. Enhanced photocatalytic reduction of Cr(VI) by manganese-doped anatase titanium dioxide. *Res Chem Intermed.* 2015;42:5413–5429.
24. Chen F, Zhang Y, Huang H. Layered photocatalytic nanomaterials for environmental applications. *Chin Chem Lett.* 2023;34(3):107523.
25. Peiris S, de Silva HB, Ranasinghe KN, Bandara SV, Perera IR. Recent development and future prospects of TiO_2 photocatalysis. *J Chin Chem Soc.* 2021;68:738–769.
26. Hu C, Huang H. Advances in piezoelectric polarization enhanced photocatalytic energy conversion. *Acta Phys - Chim Sin.* 2023;39(11):2212048.
27. Yun HJ, Lee H, Kim ND, Yi J. Characterization of photocatalytic performance of silver deposited TiO_2 nanorods. *Electrochem Commun.* 2009;11:363–366.
28. Wang Z-C, Shui H-F. Effect of PO_4^{3-} and PO_4^{3-}–SO_4^{2-} modification of TiO_2 on its photocatalytic properties. *J Mol Catal Chem.* 2007;263:20–25.
29. Wongsalee T, Jongsomjit B, Praserthdam P. Effect of zirconia-modified Titania consisting of different phases on characteristics and catalytic properties of Co/TiO_2 catalysts. *Catal Lett.* 2006;108:55–61.
30. da Silva AFV, Cesca K, Ambrosi A, Zin G, Di Luccio M, Oliveira JV. An expedite facile method for modification of PVDF membranes with polydopamine and TiO_2 to improve water permeation. *Mater Lett.* 2022;324:132611.
31. Mahović Poljaček S, Tomašegović T, Strižić Jakovljević M, Donevski D. Surface modification and properties of thin ink films with added TiO_2 and ZnO nanoparticles applied on paperboard substrates. *Materials.* 2023;16(2):478.
32. Borowska E, Gomes JF, Martins RC, Quinta-Ferreira RM, Horn H, Gmurek M. Solar photocatalytic degradation of sulfamethoxazole by TiO_2 modified with noble metals. *Catalysts.* 2019;9(6):500.
33. Kong D, Tan JZY, Yang F, Zeng J, Zhang X. Electrodeposited Ag nanoparticles on TiO_2 nanorods for enhanced UV visible light photoreduction CO_2 to CH_4. *Appl Surf Sci.* 2013;277:105–110.
34. Liu H, Dong X, Li G, Su X, Zhu Z. Synthesis of C, Ag co-modified TiO_2 photocatalyst and its application in waste water purification. *Appl Surf Sci.* 2013;271:276–283.
35. Xi Z-Y, Xu Y-Y, Zhu L-P, Wang Y, Zhu B-K. A facile method of surface modification for hydrophobic polymer membranes based on the adhesive behavior of poly(DOPA) and poly(dopamine). *J Membr Sci.* 2009;327:244–253.
36. An P, Zuo F, Li X, et al. A bio-inspired polydopamine approach to preparation of gold-coated Fe_3O_4 core-shell nanoparticles: synthesis, characterization and mechanism. *Nano.* 2013;8(6):21–33.
37. An J-R, Wang Y, Dong W-W, et al. Efficient visible-light photoreduction of CO_2 to CH_4 over an Fe-based metal–organic framework (PCN-250-Fe_3) in a solid–gas mode. *ACS Appl Energy Mater.* 2022;5:2384–2390.
38. Hu A, Liang R, Zhang X, et al. Enhanced photocatalytic degradation of dyes by TiO_2 nanobelts with hierarchical structures. *J Photochem Photobiol Chem.* 2013;256:7–15.
39. Wang L, Zhou H, Zhang H, Song Y, Zhang H, Qian X. SiO_2@TiO_2 core@shell nanoparticles deposited on 2D-layered $ZnIn_2S_4$ to form a ternary heterostructure for simultaneous photocatalytic hydrogen production and organic pollutant degradation. *Inorg Chem.* 2020;59:2278–2287.

40. Chen C, Wang N, Zhou P, San H, Wang K, Chen X. Electrochemically reduced graphene oxide on well-aligned titanium dioxide nanotube arrays for betavoltaic enhancement. *ACS Appl Mater Interfaces*. 2016;8:24638–24644.
41. Zhang Q, Ye S, Chen X, Song X, Li L, Huang X. Photocatalytic degradation of ethylene using titanium dioxide nanotube arrays with Ag and reduced graphene oxide irradiated by γ-ray radiolysis. *Appl Catal B Environ*. 2017;203:673–683.
42. Chen C, Liu P, Xia H, et al. Photocatalytic cleavage of β-O-4 ether bonds in lignin over Ni/TiO_2. *Molecules*. 2020;25(9):2109.
43. Ren H-T, Han J, Li T-T, Sun F, Lin J-H, Lou C-W. Visible light-induced oxidation of aqueous arsenite using facile Ag_2O/TiO_2 composites: performance and mechanism. *J Photochem Photobiol Chem*. 2019;377:260–267.
44. Yang L, Wang F, Shu C, Liu P, Zhang W, Hu S. An in-situ synthesis of $Ag/AgCl/TiO_2$/ hierarchical porous magnesian material and its photocatalytic performance. *Sci Rep*. 2016;6:21617.
45. Saleh R, Taufik A, Prakoso SP. Fabrication of Ag_2O/TiO_2 composites on nanographene platelets for the removal of organic pollutants: influence of oxidants and inorganic anions. *Appl Surf Sci*. 2019;480:697–708.
46. Yang O-Y, Gao X-J, Qi G-D, et al. Dye-anchoring strategy with a metal–organic framework for a highly efficient visible-light-driven photocatalytic CO_2 reduction through the solid–gas mode. *ACS Appl Energy Mater*. 2022;6:334–341.
47. Azam M, Kumar U, Olowoyo JO, et al. Dinuclear uranium(vi) salen coordination compound: an efficient visible-light-active catalyst for selective reduction of CO_2 to methanol. *Dalton Trans*. 2020;49:17243–17251.

Hongzhong Zhang received a Ph.D. degree from Beijing University of Science and Technology in 2005. He is a professor in the School of Materials and Chemical Engineering of Zhengzhou University of Light Industry, a leader in key disciplines of environmental engineering in Henan Province, and a former chair of the National Natural Science Foundation of China. He is mainly engaged in the research of photocatalysis and membrane separation coupling technology and green homogeneous catalysis technology.

Jun Li received his Ph.D. degree from Wuhan University of Technology in 2019 and is an associate professor at Zhengzhou University. He has presided over the National Natural Science Foundation of China Youth Project and the China Postdoctoral Science Foundation. In recent years, he has been mainly engaged in the structural design, in-situ characterization of nanocatalysts and their application in the field of photocatalysis and electrocatalysis.

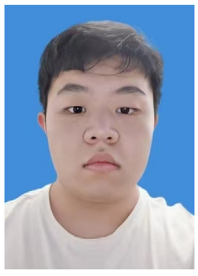

Feng Yue entered the School of Materials and Chemical Engineering of Zhengzhou University of Light Industry in 2021, joined Professor Hongzhong Zhang's research group and studied for a master's degree in resources and environment. The main research topics are the synthesis of nanocatalysts and photocatalytic CO_2 reduction at the gas-solid interface.